The influence of the magnetic field on running penumbral waves in the solar chromosphere

Jess, D. B., Reznikova, V. E., Van Doorsselaere, T., Keys, P. H., & MacKay, D. H. (2013). The influence of the magnetic field on running penumbral waves in the solar chromosphere. *Astrophysical Journal*, *779*(2), 1-11. https://doi.org/10.1088/0004-637X/779/2/168

Published in:
Astrophysical Journal

Document Version:
Publisher's PDF, also known as Version of record

Queen's University Belfast - Research Portal:
Link to publication record in Queen's University Belfast Research Portal

Publisher rights
© 2013 The American Astronomical Society. All rights reserved.

General rights
Copyright for the publications made accessible via the Queen's University Belfast Research Portal is retained by the author(s) and / or other copyright owners and it is a condition of accessing these publications that users recognise and abide by the legal requirements associated with these rights.

Take down policy
The Research Portal is Queen's institutional repository that provides access to Queen's research output. Every effort has been made to ensure that content in the Research Portal does not infringe any person's rights, or applicable UK laws. If you discover content in the Research Portal that you believe breaches copyright or violates any law, please contact openaccess@qub.ac.uk.

Download date:04. May. 2023

The Astrophysical Journal, 779:168 (11pp), 2013 December 20 doi:10.1088/0004-637X/779/2/168
© 2013. The American Astronomical Society. All rights reserved. Printed in the U.S.A.

THE INFLUENCE OF THE MAGNETIC FIELD ON RUNNING PENUMBRAL WAVES IN THE SOLAR CHROMOSPHERE

D. B. Jess[1,2], V. E. Reznikova[1], T. Van Doorsselaere[1], P. H. Keys[2,3], and D. H. Mackay[4]
[1] Center for Mathematical Plasma Astrophysics, Department of Mathematics, KU Leuven, Celestijnenlaan 200B bus 2400, B-3001 Heverlee, Belgium; d.jess@qub.ac.uk
[2] Astrophysics Research Centre, School of Mathematics and Physics, Queen's University Belfast, Belfast BT7 1NN, UK
[3] Solar Physics and Space Plasma Research Centre (SP^{2}RC), University of Sheffield, Hicks Building, Hounsfield Road, Sheffield S3 7RH, UK
[4] School of Mathematics and Statistics, University of St Andrews, St Andrews KY16 9SS, UK
Received 2013 April 30; accepted 2013 October 29; published 2013 December 3

ABSTRACT

We use images of high spatial and temporal resolution, obtained using both ground- and space-based instrumentation, to investigate the role magnetic field inclination angles play in the propagation characteristics of running penumbral waves in the solar chromosphere. Analysis of a near-circular sunspot, close to the center of the solar disk, reveals a smooth rise in oscillatory period as a function of distance from the umbral barycenter. However, in one directional quadrant, corresponding to the north direction, a pronounced kink in the period–distance diagram is found. Utilizing a combination of the inversion of magnetic Stokes vectors and force-free field extrapolations, we attribute this behavior to the cut-off frequency imposed by the magnetic field geometry in this location. A rapid, localized inclination of the magnetic field lines in the north direction results in a faster increase in the dominant periodicity due to an accelerated reduction in the cut-off frequency. For the first time, we reveal how the spatial distribution of dominant wave periods, obtained with one of the highest resolution solar instruments currently available, directly reflects the magnetic geometry of the underlying sunspot, thus opening up a wealth of possibilities in future magnetohydrodynamic seismology studies. In addition, the intrinsic relationships we find between the underlying magnetic field geometries connecting the photosphere to the chromosphere, and the characteristics of running penumbral waves observed in the upper chromosphere, directly supports the interpretation that running penumbral wave phenomena are the chromospheric signature of upwardly propagating magneto-acoustic waves generated in the photosphere.

Key words: magnetohydrodynamics (MHD) – methods: numerical – Sun: atmosphere – Sun: chromosphere – Sun: oscillations – Sun: photosphere

Online-only material: color figures

1. INTRODUCTION

Waves and oscillations manifesting in the immediate vicinity of sunspots have been known for over 40 yr (Beckers & Tallant 1969). Early work on oscillatory phenomena in sunspot structures helped validate the detection of long-period oscillations, which are generated by the response of the umbral photosphere to the five minute *p*-mode global oscillations (Thomas et al. 1982; Lites 1992). While oscillations in solar active regions are dominated by periodicities intrinsically linked to the global *p*-mode spectrum, a wealth of alternative wave periods can also be identified in the sunspot locality spanning three orders of magnitude, from several seconds (Jess et al. 2007) to in excess of one hour (Demchenko et al. 1985).

The first observational evidence of running penumbral waves (RPWs) came from Giovanelli (1972) and Zirin & Stein (1972), who detected concentric intensity waves propagating outward through the penumbra of a sunspot. These waves, deemed to be acoustic modes, were observed to propagate with a phase velocity of 10–20 km s^{-1} and exhibited intensity fluctuations in the range 10%–20%. Brisken & Zirin (1997) and Kobanov & Makarchik (2004) have since revealed how the frequencies and phase speeds of RPWs are largest (3 mHz, 40 km s^{-1}) at the inner penumbral boundary, decreasing to their lowest values (1 mHz, 10 km s^{-1}) at the outer penumbral edge. Additionally, Kobanov (2000) has shown that the propagation of RPWs can be observed in the chromosphere up to $\sim$15″ ($\sim$10,000 km) from the outer edge of the penumbral boundary, suggesting the quiet-Sun *p*-mode oscillations dominate at greater distances, hence overpowering the signatures of any remaining RPWs.

The origin of RPWs has been under intense debate ever since their discovery, with current research attempting to address whether they are trans-sunspot waves of purely chromospheric origin (e.g., Tziotziou et al. 2006, 2007 and references therein) or the chromospheric signature of upwardly propagating *p*-mode waves (Christopoulou et al. 2000, 2001; Georgakilas et al. 2000; Centeno et al. 2006). The sequence of studies by Christopoulou et al. (2000, 2001) and Georgakilas et al. (2000) employed multi-height imaging and Doppler velocity measurements to examine the phase lag between sunspot oscillations at different layers of the lower solar atmosphere. Through examination of two-dimensional power maps and the resulting spatial coherence, the authors interpreted the correlation between umbral oscillations at various atmospheric heights and simultaneous RPWs as a strong indication that RPWs are excited by upwardly propagating photospheric umbral oscillations. More recently, Tziotziou et al. (2006, 2007) employed similar multi-height imaging and spectroscopy to investigate the coupling between umbral and penumbral oscillations using spectral, phase-difference, and coherence analysis techniques. However, the authors detected large jumps in the oscillation period and the intensity-velocity phase difference at the umbra–penumbra boundary; as a result, they were unable to convincingly support the upward-propagating *p*-mode wave scenario. Conversely, Kobanov et al. (2006) examined chromospheric velocity oscillations in sunspot penumbrae, and

concluded that RPWs are the observational signature of slow-mode waves propagating along expanding magnetic field lines. Employing two-dimensional mapping of power and oscillatory period, Rouppe van der Voort et al. (2003) were also able to suggest that RPW phenomena could be attributed to near-acoustic field-aligned upward-propagating waves. Bloomfield et al. (2007) also provided momentum to the interpretation that RPWs are simply a chromospheric signature of upwardly propagating acoustic waves by combining high-resolution spectra with Fourier phase-difference analysis to reveal how they readily propagate along magnetic fields in a low β (i.e., dominated by magnetic pressure) environment. In the solar photosphere, the strong magnetic field strengths associated with sunspot umbrae result in a large magnetic pressure (i.e., $\beta \ll 1$; Mathew et al. 2004). In this regime, the magnetic field is not influenced by the motion of the plasma and, as a result, tends to a potential configuration of minimal energy (Solanki et al. 1993; Borrero & Ichimoto 2011). However, the magnetic field strength decreases radially away from the sunspot umbra, rapidly causing the gas pressure to dominate toward the edge of the penumbra (i.e., $\beta > 1$; Gary 2001; Puschmann et al. 2010).

The field of magnetohydrodynamic (MHD) seismology has rapidly risen to the forefront of solar physics research in recent years. Such techniques allow the physical quantities and structures of sub-resolution solar features to be derived directly from the analysis of waveforms propagating through the local plasma (Uchida 1970; Roberts et al. 1984; Verwichte et al. 2004; McEwan et al. 2006; Banerjee et al. 2007; Van Doorsselaere et al. 2007, 2008, to name but a few). The advent of modern high-resolution ground- and space-based instrumentation has allowed MHD seismology to uncover a wide range of new solar phenomena in the lower solar atmosphere, including torsional Alfvén waves (Jess et al. 2009), sausage waves (Morton et al. 2011), oscillations in the magnetic field (Fujimura & Tsuneta 2009; Moreels & Van Doorsselaere 2013), the presence of dual oscillating modes (Morton et al. 2012), and aspects of mode conversion (Jess et al. 2012b). By studying the fundamental parameters of ubiquitous MHD wave motion in the lower solar atmosphere, we are provided with a key opportunity to probe the constituent mechanisms behind some of the most dramatic and widespread solar phenomena.

In this paper, we utilize high spatial and temporal resolution observations to investigate the propagation characteristics of RPWs in the lower solar atmosphere. We employ Fourier analysis and potential magnetic field extrapolations, in a previously unexplored way, to study the variation of RPWs in the vicinity of a near-circular sunspot and relate the derived characteristics to the spatially dependent magnetic field inclination angles of the underlying sunspot.

2. OBSERVATIONS

The observational data presented here are part of a sequence obtained during 16:10–17:25 UT on 2011 December 10 with the Dunn Solar Telescope at Sacramento Peak, New Mexico. The Rapid Oscillations in the Solar Atmosphere (ROSA; Jess et al. 2010b) and newly commissioned Hydrogen-Alpha Rapid Dynamics camera (HARDcam; Jess et al. 2012a) multiwavelength imaging systems were employed to image a location surrounding the active region NOAA 11366, positioned at heliocentric coordinates (356″, 305″), or N17.9W22.5 in the conventional heliographic coordinate system. ROSA continuum observations were acquired through a 52 Å bandpass filter centered at 4170 Å, and employed a common plate scale of 0.″069 pixel^{-1}, providing a diffraction-limited 69″ × 69″ field of view. HARDcam observations employed a 0.25 Å bandpass filter centered on the Hα line core (6562.8 Å) and utilized a spatial sampling of 0.″138 pixel^{-1}, providing a 71″ × 71″ field of view—comparable to the ROSA continuum image sequence. During the observations, high-order adaptive optics (Rimmele 2004) were used to correct wavefront deformations in real time. The acquired images were further improved through speckle reconstruction algorithms (Wöger et al. 2008) utilizing 64 → 1 and 35 → 1 restorations for the continuum and Hα images, resulting in reconstructed cadences of 2.11 s and 1.78 s, respectively. Atmospheric seeing conditions remained excellent throughout the time series. However, to insure accurate co-alignment between the bandpasses, the broadband time series were Fourier coregistered and destretched using a 40 × 40 grid, equating to a ≈1.″7 separation between spatial samples (Jess et al. 2007). Narrowband images, including those from HARDcam, were corrected by applying destretching vectors established from simultaneous broadband reference images (Reardon et al. 2008; Jess et al. 2010a). Sample images, incorporating all image processing steps, can be viewed in Figure 1.

The Helioseismic and Magnetic Imager (HMI; Schou et al. 2012) on board the *Solar Dynamics Observatory* (*SDO*; Pesnell et al. 2012) was utilized to provide simultaneous vector magnetograms of the active region NOAA 11366. The Milne–Eddington vector magnetograms were provided with a cadence of 720 s and incorporated a two-pixel spatial resolution of 1.″0. In addition, one contextual HMI continuum (6173 Å) image, acquired at 16:10 UT, was obtained for the purposes of co-aligning the HMI data with images of the lower solar atmosphere. The HMI data were processed using the standard `hmi_prep` routine, which includes the removal of energetic particle hits. Subsequently, 200″ × 200″ subfields were extracted from the processed data with a central pointing close to that of the ground-based image sequences. Using the HMI continuum context image to define absolute solar coordinates, our ground-based observations were subjected to cross-correlation techniques to provide subpixel co-alignment accuracy between the imaging sequences. To do this, the plate scales of our ground-based observations were first degraded to match that of the HMI continuum image.[5] Next, squared mean absolute deviations were calculated between the datasets, with the ground-based images subsequently shifted to best align with the HMI reference image. Following co-alignment, the maximum x- and y-displacements are both less than one tenth of an HMI pixel, or 0.″05 (≈36 km).

3. ANALYSIS AND DISCUSSION

During the two hour duration of the observing sequence, no large-scale eruptive phenomena (*GOES* A-class or above) were observed from the active region under investigation. Examination of a time-lapse movie of HARDcam Hα images revealed clear and distinctly periodic outflows along the chromospheric canopy in a direction away from the sunspot, consistent with RPW phenomena (Giovanelli 1972; Zirin & Stein 1972). The irregular shapes of typical sunspot structures, often coupled with a noncontinuous penumbral structure, result in convoluted wave patterns at increasing distances from the umbral edge (Alissandrakis et al. 1992; Tziotziou et al. 2006). However, the near-circularly symmetric nature of our observed sunspot

[5] Data analysis was performed on full-resolution (i.e., non-degraded) image sequences

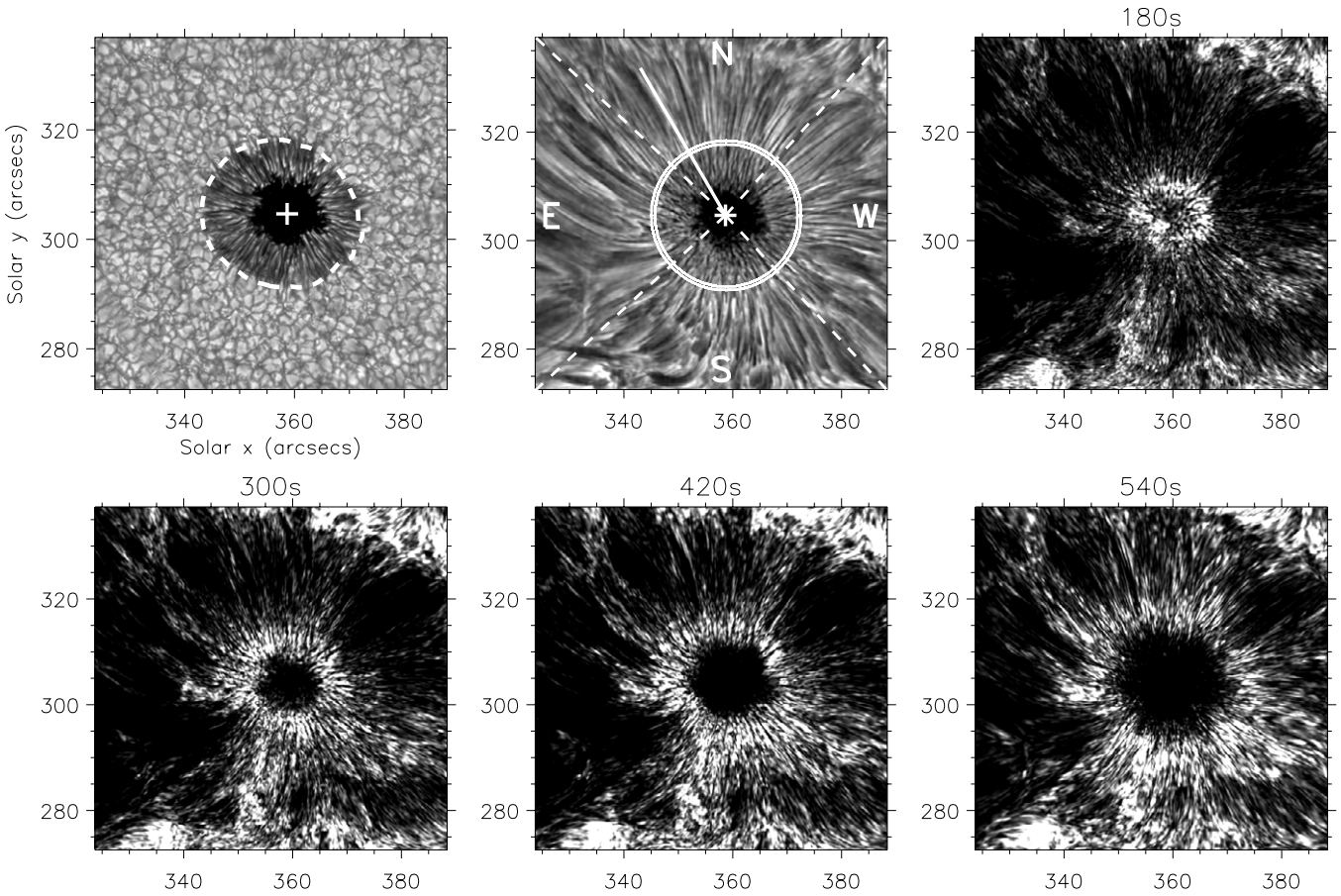

Figure 1. Simultaneous images of the blue continuum (photosphere; upper left) and Hα core (chromosphere; upper middle) acquired at 16:44 UT on 2011 December 10. A white cross marks the barycenter of the sunspot umbra, while a white dashed line in the continuum image displays the extent of the photospheric $\beta = 1$ isocontour. The white concentric circles overlaid on the chromospheric image depict a sample annulus used to extract wave characteristics as a function of distance from the umbral barycenter, while the solid white line extending into the north quadrant reveals the slice position used for the time–distance analysis displayed in Figure 2. The dashed white lines isolate the active region into four distinct regions, corresponding to the N, W, S, and E quadrants. The scale is in heliocentric coordinates where $1'' \approx 725$ km. The remaining panels display a series of chromospheric power maps extracted through Fourier analysis of the Hα time series, indicating the locations of high oscillatory power (white) with periodicities equal to 180, 300, 420, and 540 s. As the period of the wave becomes longer, it is clear that the location of peak power expands radially away from the umbral barycenter.

revealed a wealth of propagating wave fronts at distances far exceeding the outer penumbral edge.

To verify the presence of wave phenomena in our Hα field of view, we employed a Fourier-based filtering algorithm to isolate and regenerate a new time series which had been decomposed into frequency bins, each separated by 30 s, and corresponding to periodicities of 1–11 minutes. Each Fourier filter bin was peaked at 60, 90, 120,. . ., 660 s, and incorporated a Gaussian-profiled window spanning a half-width at half-maximum of $\pm$15 s. We must stress that our Fourier filtering algorithm acts only as a frequency (ω) filter. Our algorithm does not make any assumptions regarding the spatial scales associated with a particular frequency and, as a result, performs no filtering on the spatial wavenumber (k). Examination of the filtered time series clearly revealed that oscillatory signatures with longer periodicities occurred at increasing distances from the sunspot umbra and propagated with diminishing phase speeds. To quantify these characteristics, time–distance analysis was employed (see, e.g., De Moortel et al. 2002; Jess et al. 2012a). A sample slice position is displayed as a solid white line extending in the northeast direction of the Hα sunspot depicted in Figure 1. The resulting time–distance diagrams, for the filtered time series corresponding to the 3, 4, 5, and 6 minute Fourier windows, are displayed in the upper and middle panels of Figure 2. The propagating oscillatory signatures, visible as recurring white and black diagonal bands, clearly show how longer period oscillations occur more dominantly at further distances from the sunspot umbra (marked as 0 Mm on the y-axis). Importantly, these propagating waves appear to be continuous in time, indicating they are driven by a regular and powerful source. Furthermore, the gradient of the diagonal bands provides an indication of the horizontal (i.e., parallel to the solar surface) phase speed of the propagating waves. A best-fit line reveals phase speeds of $\approx$15.5, $\approx$12.6, $\approx$10.4, and $\approx$8.8 km s^{-1} for the 3, 4, 5, and 6 minute Fourier windows, respectively. Employing the line-of-best-fit technique to each of the other Fourier-filtered time series reveals phase speeds spanning $\approx$18.5 km s^{-1} (60 s periodicity) to $\approx$5.6 km s^{-1} (660 s periodicity). Interestingly, the range of measured phase velocities was independent of the orientation of the time–distance slice. Regardless of the azimuthal direction in which the one-dimensional slice was placed, the observed wave periods propagated with the same phase velocities. All of the measured phase velocities are plotted as a function of oscillatory period in the lower panel of Figure 2. While the characteristics and trends displayed by the RPWs studied here are consistent with those measured in previous studies (e.g., Brisken & Zirin 1997; Kobanov & Makarchik 2004), the implementation of Fourier filtering

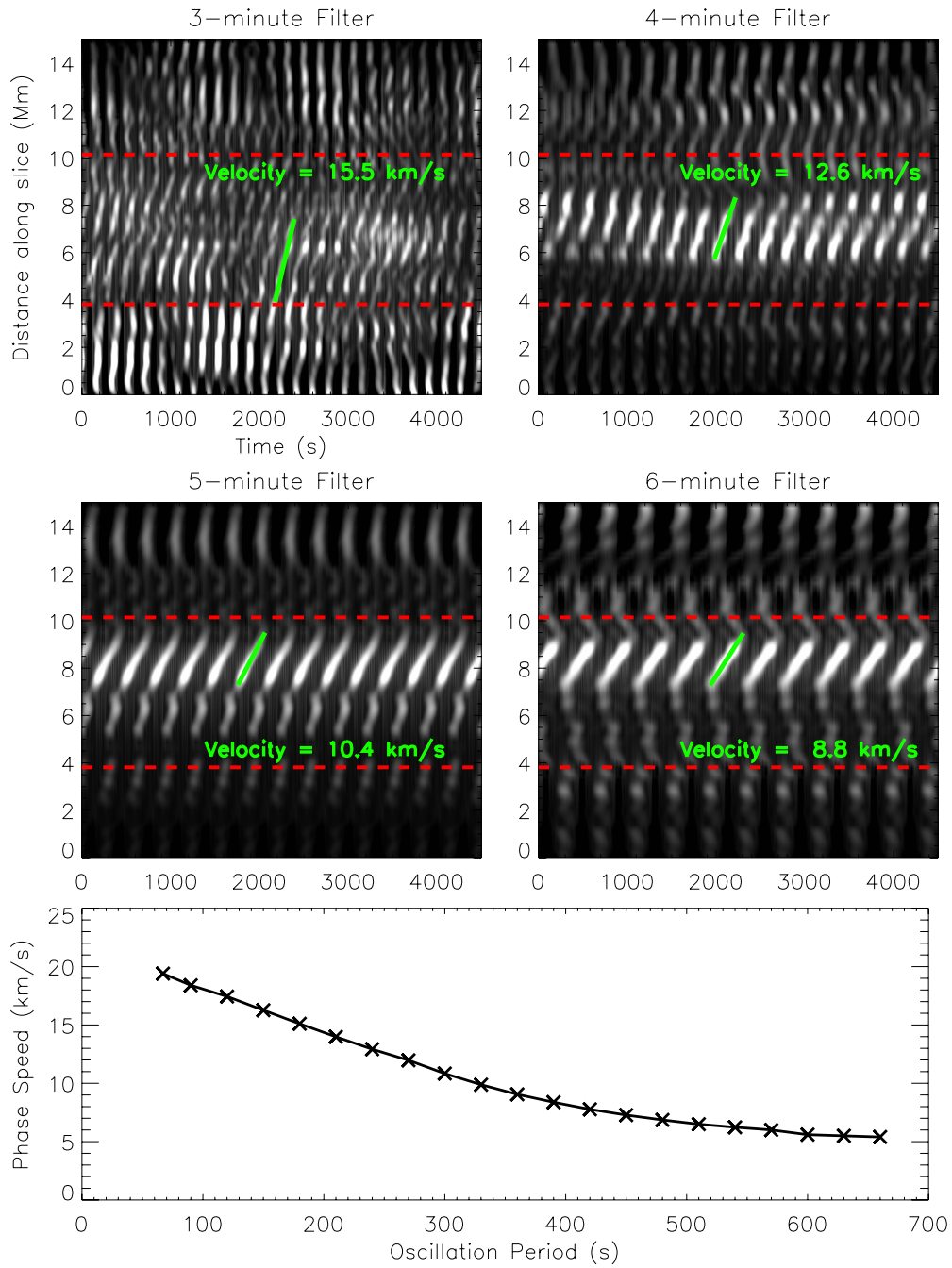

Figure 2. Time–distance diagrams corresponding to the 3 (upper-left), 4 (upper-right), 5 (middle-left), and 6 (middle-right) minute Fourier-filtered time series, where the *y*-axis corresponds to the spatial extent occupied by the slice overlaid in the upper-middle panel of Figure 1. The red horizontal dashed lines highlight the inner- and outer-penumbral boundaries at ≈3.8 and ≈10.1 Mm, respectively, from the umbral barycenter. The solid green lines highlight the lines of best fit used to calculate the period-dependent phase speeds. Each time–distance diagram consists of 150 spatial (≈15 Mm) by 2528 temporal (75 minutes) pixels^2. The lower panel displays the RPW phase speed (in km s^{-1}) as a function of oscillatory period.

(A color version of this figure is available in the online journal.)

algorithms significantly improves the accuracy of the phase velocity measurements. Each pixel in the unfiltered time series consists of the superposition of a large number of independent wave forms, each with different periodicities and phase speeds. The filtered time series removes this ambiguity and allows the exact phase velocity to be reliably extracted as a function of period and distance from the sunspot umbra.

To more closely quantify the characteristics associated with the propagating waves, Fourier-based analysis techniques were implemented on the unfiltered data. Due to the continual nature of the RPWs over the duration of our 75 minute time series, we employed the methodology of Jess et al. (2007) to apply strict Fourier analysis to the entire Hα time series, allowing the signatures of wave phenomena to be easily extracted as a function of period. The upper-right and lower panels of Figure 1 display two-dimensional power maps for periodicities equal to 180, 300, 420, and 540 s. As from the time–distance analysis shown in Figure 2, it is clear that the maximum Fourier power (displayed as bright white) for longer periodicities occurs at greater radial distances from the sunspot umbra. Due to the near-circularly symmetric nature of the sunspot under investigation, the best approach to study oscillatory behavior as a function of

radial distance is to examine the Fourier power over a series of expanding annuli. However, the center of the expanding series of annuli must first be defined. To do this, continuum images of the sunspot umbra were isolated from the surrounding plasma. A time-averaged continuum image was created by averaging all of the 4170 Å blue continuum images over the entire 75 minute duration of the dataset. Next, the umbral pixels were defined as those with an intensity below 45% of the median granulation intensity. Features brighter than this were discarded, producing an accurately defined umbral perimeter containing ∼22, 000 umbral pixels, or an area of 2.2×10^8 km^2. From here, the umbral center of gravity, or "barycenter," was established, which formed the central coordinates of the annuli used in the subsequent analysis. Here, a width of 5 pixels for each annulus was chosen and subsequent annuli were spaced by 2 pixels from the preceding annulus. Some overlap between adjacent annuli was chosen to provide continuous radial coverage of the measured parameters while still maintaining high pixel numbers to improve statistics. This was deemed essential since the number of pixels enclosed within a particular annulus is greatly reduced at smaller radii from the umbral barycenter. Therefore, either a thicker annulus could be used or more overlap could be provided between adjacent annuli. A thicker annulus was not desirable as this may artificially mask any changes in wave behavior with distance. As a result, we chose to use an overlap between adjacent annuli, which greatly assists with measurements at small distances from the umbral barycenter. This overlap was kept constant for all annuli, regardless of the distance from the umbral barycenter. A sample annulus, which is 100 pixels (∼10 Mm) from the umbral barycenter, is displayed in the upper-middle panel of Figure 1.

Examination of the power contained within the annuli reiterated that higher frequency intensity oscillations were confined to the inner penumbral edge, whereas lower frequency perturbations were dominant at greater distances from the umbral barycenter (Figure 3). The highest frequency intensity oscillations that we detected had a period ≈45 s (at a 95% confidence level), calculated by multiplying the power in the background spectrum by the values of χ^2 corresponding to the 95th percentile of the distribution (Torrence & Compo 1998; Mathioudakis et al. 2003; Jess et al. 2007). In this case, the background spectrum is assumed to be consistent with pure photon noise (i.e., normally distributed in the limit of large number statistics) and to follow a χ^2 distribution with two degrees of freedom. The longest intensity oscillation periods found, which superseded the 95% confidence criteria, were ≈1200 s, significantly under the Nyquist period of 2250 s. The upper panel of Figure 3 reveals the absolute Fourier power, which has been spatially and temporarily averaged over each individual annulus, as a function of period and distance from the umbral barycenter. Here, long-period oscillations (displayed as darker colored lines) appear to display higher oscillatory power; a direct result of larger amplitudes accompanying the longer-period waves (Didkovsky et al. 2011). Normalization of the power spectra—by the average power contained within the entire field of view for each corresponding periodicity—reveals more meaningful structural information (middle panel of Figure 3). In this plot, the vertical axis gives a direct representation of how much each periodicity displays power above its spatially and temporally averaged background. Here, the shorter-period waves (45–180 s) display their peak power at the umbral/penumbral edge, with their relative power approximately three orders of magnitude higher than the background. As distance from the umbral barycenter is increased, the peak power is dominated by further increasing periodicities, with a dominant period of ≈640 s at the outer penumbral edge.

It can clearly be seen in Figure 3 that the dominant periodicity increases significantly between the inner and outer penumbral edges. This effect has been attributed to the inclination angles of the magnetic field lines increasing as a function of distance from the sunspot umbra (Bel & Leroy 1977). As a result, the acoustic cutoff becomes heavily modified, thus allowing the free propagation of longer-period waves at increasing distances from the sunspot umbra. Bloomfield et al. (2007) displayed clear evidence of this phenomena by comparing the wave power spectra with the dispersion relations presented by Centeno et al. (2006). However, the authors employed single-slit spectroscopic measurements with a spatial resolution of 0.″8; therefore, they were unable to examine all locations within the sunspot umbra to a high degree of precision. To exploit our high spatial resolution observations, and to quantify the change in period at increasing distances from the sunspot umbra, we calculated the dominant periodicity as a function of distance from the umbral barycenter for four distinct regions of the sunspot: the north (N), west (W), south (S), and east (E) quadrants (see upper-middle panel of Figure 1). For each quadrant, the dominant periodicity was defined as the periodicity that had the most relative power within each annulus segment. It was found that the W, S, and E quadrants displayed a gradual change in the dominant period as a function of distance from the umbral barycenter (black line in the lower panel of Figure 4). However, the N quadrant displayed two distinct gradients between the inner and outer penumbral edges when displayed on a log–log scale. From the inner penumbral edge (≈3.8 Mm from the umbral barycenter) to ≈7.4 Mm from the umbral barycenter, a line of best fit reveals a periodicity, P, equal to

$$P = (53.13 \pm 1.03) D^{(0.87 \pm 0.01)}, \quad (1)$$

where 0.87 is the gradient of the line of best fit, 53.13 is the periodicity when the distance from the umbral barycenter, D, equals unity, and the errors listed are the 1σ uncertainty estimates provided by the fitting function. The second distinct gradient appears between ≈7.4 Mm and the outer penumbral edge (≈10.2 Mm) from the umbral barycenter. Here, a line of best fit allows the periodicity to be expressed as

$$P = (3.99 \pm 1.08) D^{(2.17 \pm 0.03)}. \quad (2)$$

While the general increase in period as a function of distance from the sunspot umbra has been well documented in previous studies, this is the first observational evidence of two distinct gradients present in a resulting period–distance plot (middle panel of Figure 4). Thus, there are two important questions: (1) why is the N quadrant of the sunspot different from the others and (2) what physical mechanisms are responsible for this pronounced effect? To investigate, we examined the vector magnetic field information collected by the HMI instrument. The Very Fast Inversion of the Stokes Vector (VFISV; Borrero et al. 2011) algorithm was utilized to decompose the magnetograms into components parallel (B_x and B_y) and perpendicular (B_z) to the solar surface. Specifically, the initial vector field components (filename "hmi.ME_720s_fd10" on the Joint Science Operations Center, or JSOC, catalog) provide three values for each pixel related to the field strength, inclination angle, and non-disambiguated azimuthal angle. Azimuthal disambiguation

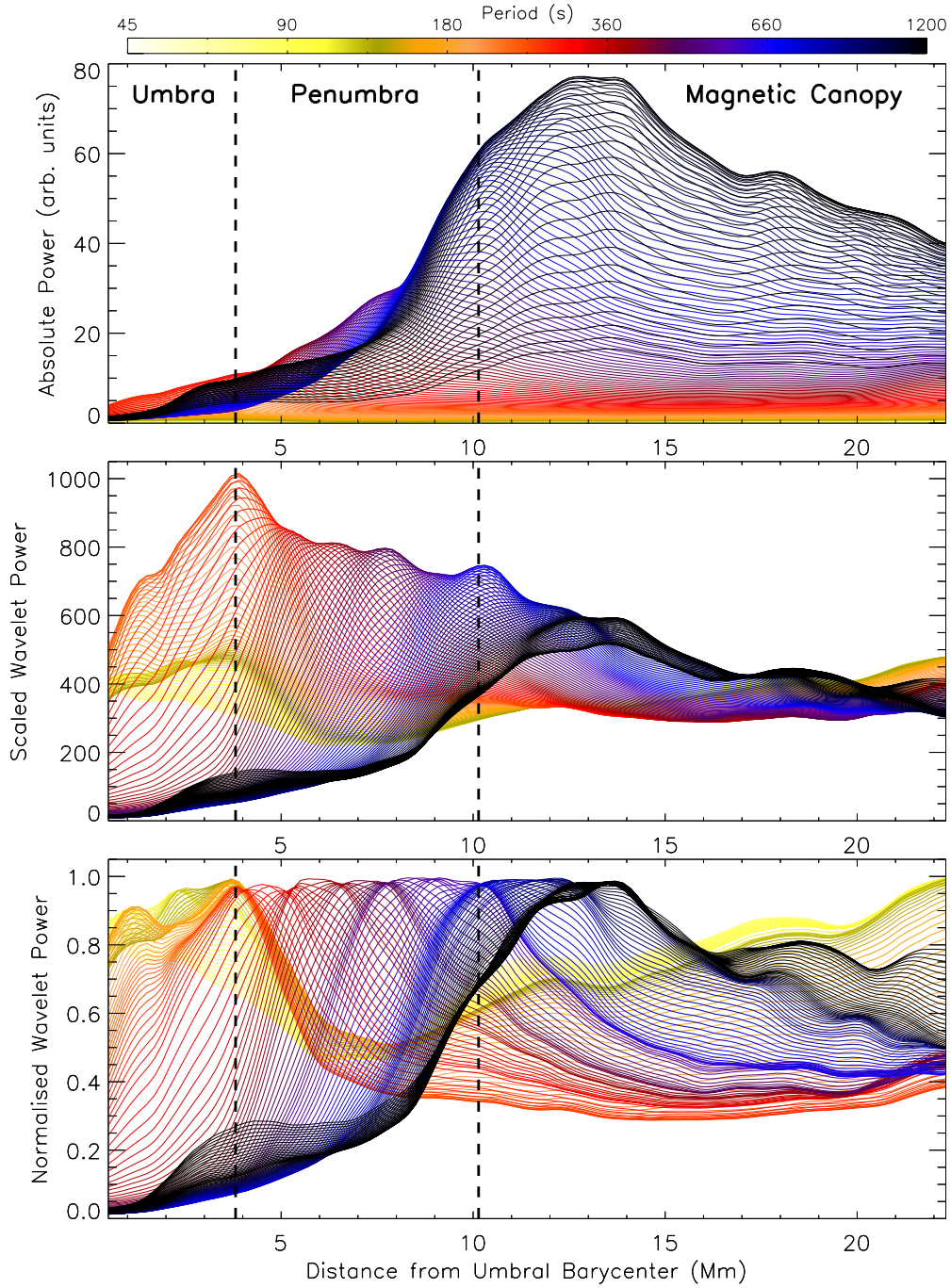

Figure 3. Top: azimuthally averaged absolute Fourier power displayed as a function of radial distance from the umbral barycenter. Middle: power spectra from the top panel normalized by the average power for that periodicity within the entire field of view. Thus, the vertical axis represents a factor of how much each period displays power above its spatially and temporally averaged background. Bottom: power spectra normalized to their own respective maxima. The vertical dashed lines represent the radial extent of the umbral and penumbral boundaries, while the graduated color spectrum, displayed at the very top, assigns display colors to a series of increasing periodicities between 45 and 1200 s.

(A color version of this figure is available in the online journal.)

of the transverse magnetic field vectors was undertaken using the algorithms of Rudenko & Anfinogentov (2011). The disambiguated vector magnetograms were subsequently transformed into line-of-sight, east–west, and north–south components (the so-called basic transformation) following the procedures outlined in the HMI users guide.[6] Finally, the transformation from the line-of-sight coordinate system into the correct heliographic projection (called either the "advanced" or "vertical/horizontal" decomposition) was performed in accordance with Gary & Hagyard (1990). Although the VFISV Milne–Eddington inversion algorithm returns a single magnetic field component, there is no doubt that the true magnetic configuration will be more complicated than that portrayed by even the relatively high resolution HMI observations. Particularly, in sunspot penumbrae, individual flux tubes have been found to show an interlocking comb configuration (Weiss et al. 2004), whereby weaker and stronger field components have different inclination angles over very

[6] Users guide available at ftp://pail.stanford.edu/pub/HMIvector/documents/vector_guide.pdf.

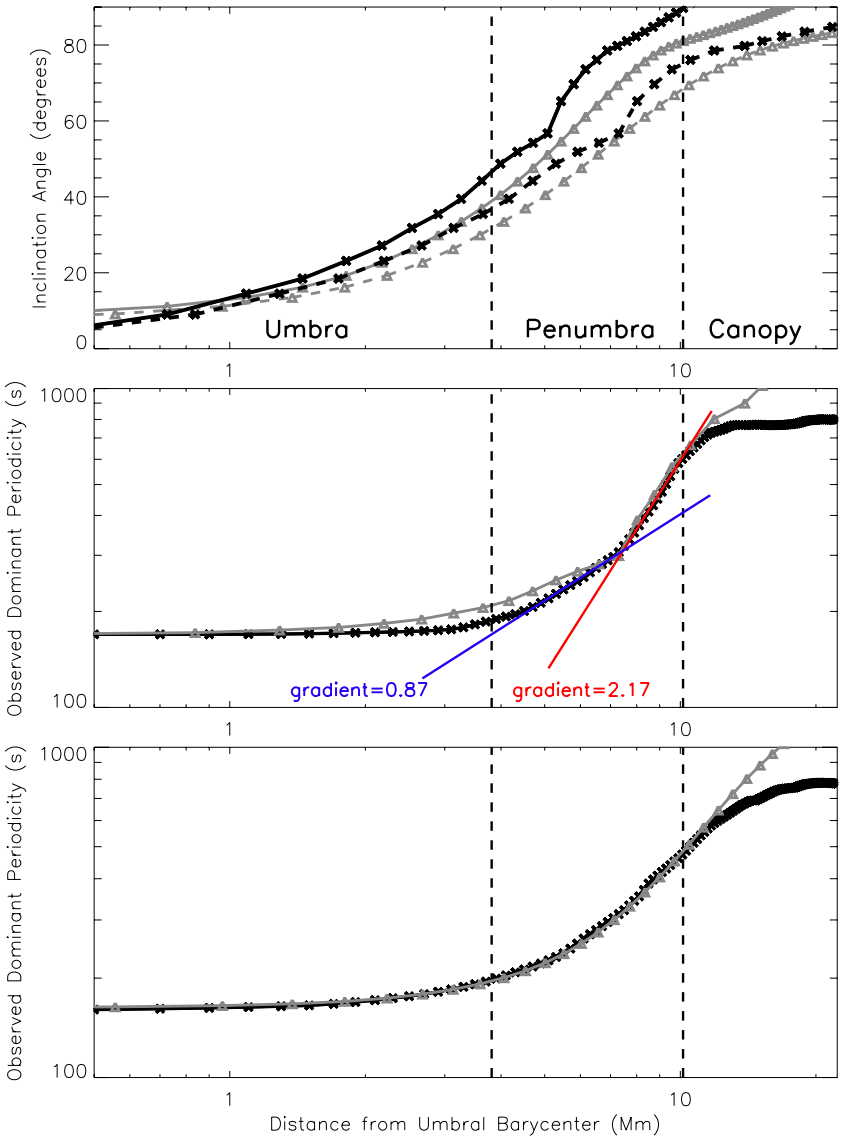

Figure 4. Average inclination angles for the N (solid black line) and W+S+E (solid gray line) quadrants are plotted as a function of photospheric distance from the umbral barycenter in the upper panel. The dashed black and gray lines correspond to the same inclination angles plotted as a function of chromospheric distance from the umbral barycenter determined through magnetic field extrapolations. The observed dominant periodicity for the N sunspot quadrant is displayed in the middle panel on a log–log scale as a function of the radial distance from the umbral barycenter (solid black line). Within the confines of the penumbra, there appear to be two distinct gradient slopes, as indicated by the blue and red lines of best fit. A solid gray line displays the acoustic cutoff period determined from the magnetic field inclination angles present in this quadrant of the sunspot. The lower panel displays the same information for the values averaged over the remaining three quadrants (W, S, and E). The vertical dashed lines indicate the inner and outer penumbral boundaries at ≈3.8 and ≈10.1 Mm, respectively.

(A color version of this figure is available in the online journal.)

short distances. In addition, the magnetic structure cannot be entirely current-free and, therefore, is also highly dynamic and constantly evolving (Thomas & Weiss 2008). However, for now we use the single field component provided by HMI as a first approximation of the dominant spatially resolved magnetic field vectors present in our observations. The derived values allowed the absolute magnetic field strength, B, to be computed for each pixel within our field of view. Importantly, the absolute magnetic field strength provided us with the ability to estimate the location of the $\beta = 1$ layer in the solar photosphere. The plasma β is traditionally defined as the ratio between the gas pressure, (P_g), and the magnetic pressure, ($P_B = B^2/8\pi$), where B is the absolute magnitude of the magnetic field strength. The plasma gas pressure was estimated using the Maltby et al. (1986) average sunspot model "M" with parameters that corresponded to the HMI magnetogram formation height of ∼300 km (Bruls et al. 1991; Norton et al. 2006; Fleck et al. 2011). A temperature, $T = 3400$ K, and hydrogen number density, $n_H = 1 \times 10^{16}$ cm^{-3}, obtained for an atmospheric height of ∼300 km from Maltby et al. (1986) were used to estimate P_g. The resulting plasma β was calculated according to $\beta = P_g/P_B = 8\pi n_H T k_B/B^2$, where k_B is the Boltzmann constant. An isocontour corresponding to the photospheric $\beta = 1$ layer is overplotted using a dashed white line on the blue continuum image displayed in the upper left panel of Figure 1. As a result, all plasma inside the isocontour is $\beta \leqslant 1$, allowing the whole sunspot structure to be considered as a low-β region.

To investigate the role that the magnetic field geometries may play in the creation of the period kink found in the N quadrant (solid black line in the middle panel of Figure 4), we utilized the potential force-free field extrapolation code of Guo et al. (2012). Following the methods detailed in Metcalf et al. (2006) and

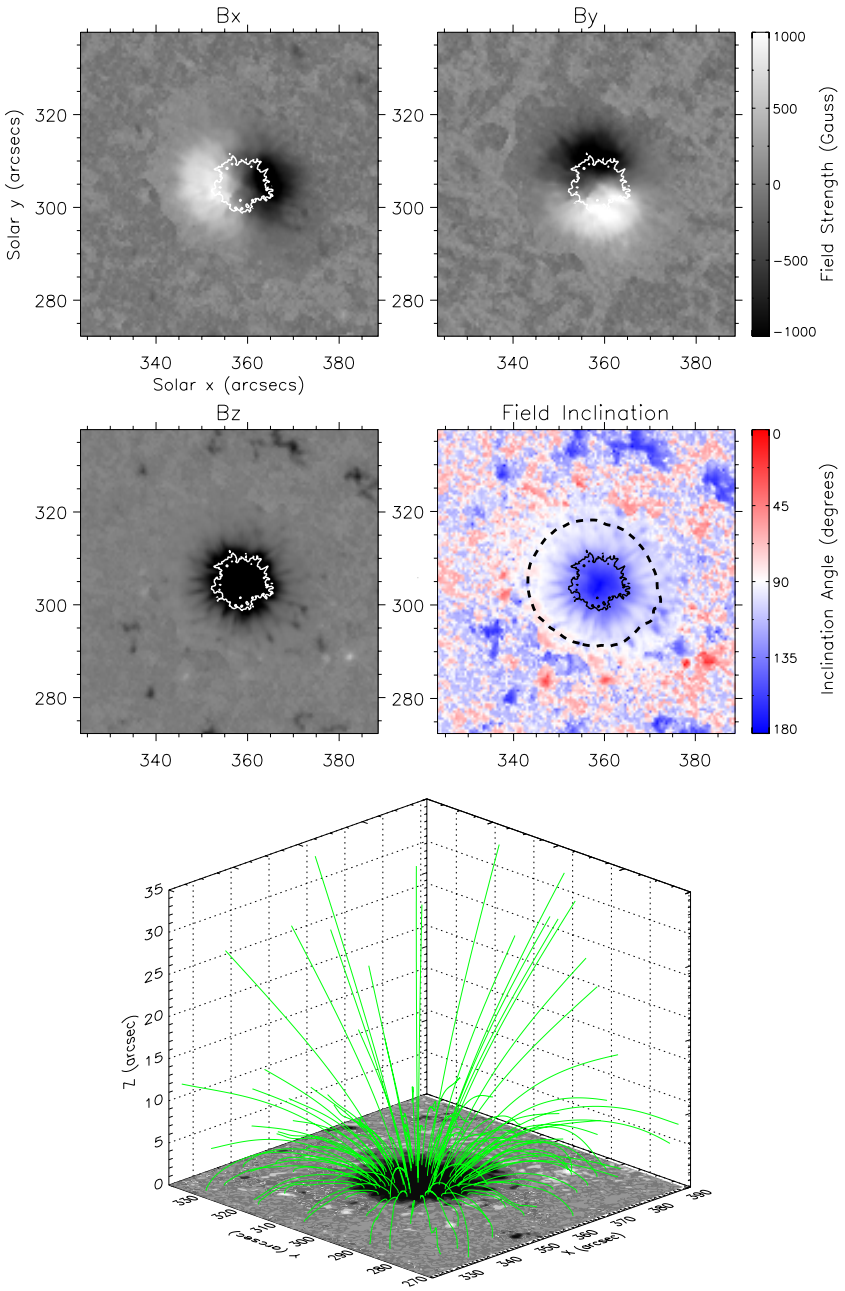

Figure 5. HMI vector field components parallel (B_x, upper left; B_y, upper right) and perpendicular (B_z, middle left) to the solar surface for NOAA 11366, where the magnetic field strength is displayed in grayscale and artificially saturated at $\pm$1000 G for clarity. The middle right panel reveals the inclination angles of the magnetic field vectors to the solar normal, while the lower panel displays the extrapolated magnetic fields (green lines) overlaid on the B_z map from an angle of 45° to the solar surface. The solid contours in each panel display the location of the inner penumbral boundary, while the dashed line in the middle right panel displays the photospheric $\beta = 1$ isocontour, which is representative of the outer penumbral boundary. The axes are displayed in heliocentric arcseconds.

(A color version of this figure is available in the online journal.)

Leka et al. (2009), magnetic field extrapolations were performed for the sunspot under investigation using the derived heliographic components as the initial conditions. Maps displaying the specific B_x, B_y, and B_z magnetic components, in addition to the field vector angles for the observational field of view under investigation, are shown in the upper and middle panels of Figure 5. Note that the inclination angles, θ, displayed in the middle right panel of Figure 5 are in the range 0°–180°, where 180° corresponds to a negative polarity with a magnetic field vector pointing toward the center of the Sun (Reznikova & Shibasaki 2012). For the purposes of displaying how the inclination angles vary as a function of radial distance, the true vector angles were recalculated so that 0° corresponds to a direction parallel to the solar normal (regardless of the absolute direction of the magnetic field vector) and 90° coincides with directions perpendicular to the solar surface. The azimuthally averaged inclination angles to the solar normal are displayed as a function of distance from the umbral barycenter for the N and W+S+E quadrants in the upper panel of Figure 4. Importantly, the magnetic field extrapolations allow us to accurately determine what spatial locations the purely photospheric HMI-derived inclination angles (middle right panel in Figure 5) correspond to once they are extrapolated to chromospheric heights. As the photospheric inclination angles increase

as a function of distance from the umbral barycenter (solid black and gray lines in the upper panel of Figure 4), one would expect that the chromospheric counterpart of these photospheric magnetic fields would lie at ever-increasing distances from the umbral barycenter. By tracing the photospheric magnetic field lines (acquired at a formation height of ~300 km; Bruls et al. 1991; Norton et al. 2006; Fleck et al. 2011) up to a chromospheric height corresponding to the core of the Hα line (~1700 km; Vernazza et al. 1981; Leenaarts et al. 2012), we are able to display how the photospheric field inclinations would behave when displayed as a function of chromospheric distance. In order to maximize the accuracy of this procedure, the magnetic field lines were traced along incrementally connected three-dimensional (3D) vectors obtained via the potential magnetic field extrapolations, thus increasing the accuracy over a more simplistic straight-line approximation between photospheric and chromospheric heights. Often the selection of a specific Hα formation height is fraught with difficulties, particularly in regions of high magnetic field strengths such as sunspots and pores. Leenaarts et al. (2012) have made considerable progress in recent years using full 3D simulations of chromospheric plasma, including environments with a low plasma β (i.e., dominated by magnetic pressure). These authors found an average Hα formation height that varies between 1100 and 1900 km depending on the local optical depth. Particularly, there is likely to be small chromospheric opacity in our observations of the umbral core, implying we are seeing farther down into the photospheric layer (Rutten 2007). From the Hα image displayed in Figure 1, it is clear that the sunspot umbra is dark and well defined, suggesting that the opacity is greatly reduced and that the formation height may be as low as 1100 km. However, in the penumbra and chromospheric canopy regions, where we actually report on the characteristics of the RPWs, the opacity and the plasma β will be much greater. Thus, in these regions, the narrowband (0.25 Å) Hα core formation height is likely to be higher and similar to the ~1700 km proposed by Leenaarts et al. (2012).

The upper panel of Figure 4 displays the HMI-derived inclination angles for both photospheric (solid black and gray lines) and chromospheric (dashed black and gray lines) distances. It is clear that when plotted on a chromospheric distance scale, the changes in the inclination angles occur at greater distances from the umbral barycenter when compared to the photospheric distance scale. Furthermore, a distinct jump in the inclination angle for the N quadrant is visible at a photospheric distance of ≈5.1 Mm, suggesting the inclination angle changes rapidly over a very short distance. The physical reason for this jump is unclear. Careful examination of the inclination map (middle right panel of Figure 5) reveals that a large fraction of the sunspot circumference displays prominent "spines" of low inclination angles radially extending outward from the umbra. These spines are visible in the middle right panel of Figure 5 as blue (i.e., more vertically orientated) structures extending radially outward from the sunspot umbra. A more detailed examination of these spine structures reveals they preferentially correspond to bright penumbral filaments, as observed in both the ROSA and HMI continuum images. This link between vertical magnetic fields and bright penumbral filaments is in direct agreement with the work of Hofmann et al. (1993) and Langhans et al. (2005, 2007). However, in the N quadrant, these spines appear to be less pronounced and more curved, resulting in a more rapid, localized change in the magnetic field inclination angle as a function of distance from the umbral barycenter. When this kink in the inclination angle is mapped to a chromospheric distance scale, it occurs at a distance of ≈7.4 Mm (dashed black line in the upper panel of Figure 4)—exactly the point where we observe a kink in the period–distance diagram for the RPWs. This technique allows us to directly compare the observed chromospheric wave phenomena with photospheric magnetic field inclination angles derived from HMI vector magnetograms. The output of the magnetic field extrapolations can be viewed in the lower panel of Figure 5. The near-potential configuration of the sunspot, in addition to its near-circularly symmetric composition, results in magnetic field lines expanding outward in all directions from the underlying umbra.

Magnetic field inclination angles play an important role in the propagation of magneto-acoustic wave modes. In the presence of gravitational fields, they can only propagate upward at frequencies above the acoustic cutoff, f_c, defined as

$$f_c = \frac{g\gamma}{2\pi C_s}, \tag{3}$$

where $C_s = \sqrt{\gamma RT/\mu}$ is the local sound speed, T is the temperature, γ is the ratio of specific heats, μ is the mean molecular weight, and R is the gas constant. Bel & Leroy (1977) predicted that in regions of low-β plasma, an effective gravity, g, on a particular magnetic field line can be expressed as

$$g = g_0 \times \cos\theta, \tag{4}$$

where the gravitational acceleration, g_0, is decreased by the cosine of the inclination angle, θ, with respect to the solar normal. From Equation (3), it is clear that the maximum cutoff frequency is determined by the minimum values of θ (to maximize the numerator) and T (to minimize the denominator) along the path of wave propagation. As a result, both parameters (θ and T) should be taken at the level which corresponds to the minimum temperature along a particular field line: the "cutoff height." We assume that both the inclination angle and the temperature will increase beyond the cutoff height; therefore, the cutoff height will define the frequency spectrum of waves that can propagate beyond the temperature-minimum level. According to the atmospheric sunspot models of Maltby et al. (1986), the temperature-minimum region is located 280–530 km above the continuum optical depth $\tau_{500\,\mathrm{nm}} = 1$. Here, we adopt the cutoff height as the formation height of the HMI magnetograms (~300 km).

The spatially dependent cutoff frequencies were calculated using a minimum temperature, $T = 3400$ K, $\mu = 1.3$ g mol^{-1}, $g_0 = 274$ m s^{-2}, $R = 8.31$ J mol^{-1} K^{-1}, and $\gamma = 5/3$ for an ideal monoatomic gas; g_0 was then combined with the extrapolated cos θ terms to find the spatially dependent effective gravity. The azimuthally averaged cutoff periods for the N and W+S+E sunspot quadrants are displayed as a function of chromospheric distance from the umbral barycenter using gray lines in the middle and lower panels of Figure 4, respectively. The kink present in the inclination angle (N quadrant) diagram in the upper panel of Figure 4 results in a similar kink in the corresponding cutoff period (gray line in the middle panel of Figure 4). Contrarily, the more smoothly varying inclination angles present in the W+S+E quadrants results in an equally smooth variation in the resulting cutoff period (gray line in the lower panel of Figure 4). It is clear that the observed dominant periodicities closely follow the acoustic cutoff period, thus remaining consistent with the work of Bel & Leroy (1977) and highlighting the importance of being able to accurately

relate chromospheric phenomena to the underlying photospheric magnetic field geometry.

From the structure of a sunspot, it is clear that RPWs observed at increasing distances from the umbral barycenter will have traveled along magnetic field lines that are more inclined to the solar normal. This has direct consequences on the acoustic cutoff period; longer periods are found at increasing distances from the umbral barycenter, producing a gradual change in the observed period when the magnetic field inclination angles are slowly varying (see, e.g., the black line in the lower panel of Figure 4). However, when a more rapidly varying magnetic field geometry is present, such as that corresponding to the N region of the sunspot under investigation, the resulting period–distance diagram (middle panel of Figure 4) clearly reflects this magnetic complexity by revealing a distinct kink in the resulting relationship. Here, a rapid, localized inclination of the magnetic field lines results in a faster increase in the dominant periodicity due to the reduced cutoff frequency. The fact that the observed wave periods can be accurately constrained by the magnetic field inclination angles and the associated cutoff period implies—at least for the sunspot under investigation—that its low-β nature allows it to be accurately modeled using force-free magnetic field extrapolations. Ultimately, this provides the ability to directly relate chromospheric phenomena to the underlying photospheric magnetic field complexity. Interestingly, the magnetograms displayed in Figure 5 also shine light on the intricate structuring present in the Hα image displayed in the upper middle panel of Figure 1. It appears that the Hα canopy structure has termination points visible in the northwest and southeast corners of the field of view. Figure 5 clearly reveals that these regions contain pockets of high unipolar magnetic field strength, which are often the locations of concentrated groups of magnetic bright points (Jess et al. 2010a). In addition, these features typically give rise to localized regions of high oscillatory power (e.g., the northwest and southeast corners of the Fourier power maps in Figure 1), which explains the presence of such oscillatory phenomena in these corners of the field of view. The termination of Hα canopy structures and the manifestation of high oscillatory power are consistent with previous studies of magnetic bright point groups (Jess et al. 2009, 2012b; Lawrence et al. 2011).

We also suggest that the reverse approach can be implemented to obtain key information on the magnetic field geometries surrounding sunspots. In such a "reverse" regime, the presence of a kink in a period–distance diagram, the precise location of the kink, and the gradients before and after the kink can all be used to provide valuable structural information related to the underlying magnetic field geometry. By establishing the wave periods, the spatial variance of the magnetic field strengths, and the cutoff periods present in the observations, the orientation of the underlying magnetic fields can be estimated directly. Importantly, the derived relationships between the underlying magnetic field geometries connecting the photosphere to the chromosphere, and the characteristics of RPWs observed in the upper chromosphere, directly support the interpretation of Christopoulou et al. (2000, 2001) that these phenomena are the chromospheric signature of upwardly propagating magneto-acoustic waves generated in the photosphere.

4. CONCLUDING REMARKS

We have combined one of the highest resolution solar instruments currently available with a series of detailed computations to show that the observed variations in RPW periods can be explained by the influence of the low-frequency acoustic cutoff period. In the vicinity of the sunspot, the dominant periods are determined by the acoustic cutoff, which is directly influenced by the local inclination angles of the magnetic fields to the solar normal. Waves that pass this filtering selection criteria are then allowed to be channeled into the chromosphere where they are observed as RPWs. A kink in the period–distance relationship for RPWs may be found if the magnetic field geometry changes rapidly over a relatively short distance. This kink can be more or less pronounced depending on the field inclination angles, and their associated rate of change, present in a particular locality. Importantly, this means that the spatial distribution of dominant wave periods directly reflects the magnetic geometry of the underlying sunspot, thus opening up a wealth of possibilities in future MHD seismology studies.

Using dedicated Fourier filtering algorithms, we have accurately measured the period-dependent phase velocity of RPWs. The shortest period waves ($\sim$60 s) have a phase velocity of $\approx$18.5 km s^{-1}, while the longest period waves ($\sim$660 s) exhibit a phase velocity of $\approx$5.6 km s^{-1}. In addition, the intrinsic relationships we find between the underlying magnetic field geometries connecting the photosphere to the chromosphere, and the characteristics of RPWs observed in the upper chromosphere, directly support the interpretation that these phenomena are the chromospheric signature of upwardly propagating magneto-acoustic waves generated in the photosphere.

D.B.J. thanks the European Commission and the Fonds Wetenschappelijk Onderzoek (FWO) for the award of a Marie Curie Pegasus Fellowship during which this work was initiated, in addition to the UK Science and Technology Facilities Council (STFC) for the award of an Ernest Rutherford Fellowship which allowed the completion of this project. The research carried out by V.E.R. is partly supported by grant MC FP7-PEOPLE-2011-IRSES-295272. T.V.D. acknowledges funding from the Odysseus Programme of the FWO Vlaanderen and from the EU's 7th Framework Programme as an ERG with grant number 276808. P.H.K. and D.H.M. are grateful to STFC for research support. This research has been funded by the Interuniversity Attraction Poles Programme initiated by the Belgian Science Policy Office (IAP P7/08 CHARM). All authors thank the anonymous referee for their helpful comments and detailed knowledge which significantly improved this manuscript.

Facilities: Dunn (HARDcam, ROSA), *SDO* (HMI)

REFERENCES

Alissandrakis, C. E., Georgakilas, A. A., & Dialetis, D. 1992, SoPh, 138, 93
Banerjee, D., Erdélyi, R., Oliver, R., & O'Shea, E. 2007, SoPh, 246, 3
Beckers, J. M., & Tallant, P. E. 1969, SoPh, 7, 351
Bel, N., & Leroy, B. 1977, A&A, 55, 239
Bloomfield, D. S., Lagg, A., & Solanki, S. K. 2007, ApJ, 671, 1005
Borrero, J. M., & Ichimoto, K. 2011, LRSP, 8, 4
Borrero, J. M., Tomczyk, S., Kubo, M., et al. 2011, SoPh, 273, 267
Brisken, W. F., & Zirin, H. 1997, ApJ, 478, 814
Bruls, J. H. M. J., Lites, B. W., & Murphy, G. A. 1991, in Solar Polarimetry, ed. L. J. November (Sunspot, NM: National Solar Observatory), 444
Centeno, R., Collados, M., & Trujillo Bueno, J. 2006, ApJ, 640, 1153
Christopoulou, E. B., Georgakilas, A. A., & Koutchmy, S. 2000, A&A, 354, 305
Christopoulou, E. B., Georgakilas, A. A., & Koutchmy, S. 2001, A&A, 375, 617
Demchenko, B. I., Minasyants, G. S., Makarenko, N. G., & Obashev, S. O. 1985, ATsir, 1360, 3
De Moortel, I., Hood, A. W., Ireland, J., & Walsh, R. W. 2002, SoPh, 209, 89
Didkovsky, L., Judge, D., Kosovichev, A. G., Wieman, S., & Woods, T. 2011, ApJL, 738, L7

Fleck, B., Couvidat, S., & Straus, T. 2011, SoPh, 271, 27
Fujimura, D., & Tsuneta, S. 2009, ApJ, 702, 1443
Gary, G. A. 2001, SoPh, 203, 71
Gary, G. A., & Hagyard, M. J. 1990, SoPh, 126, 21
Georgakilas, A. A., Christopoulou, E. B., & Koutchmy, S. 2000, A&A, 363, 306
Giovanelli, R. G. 1972, SoPh, 27, 71
Guo, Y., Ding, M. D., Liu, Y., et al. 2012, ApJ, 760, 47
Hofmann, A., Schmidt, W., Balthasar, H., Tarbell, T. T., & Frank, Z. A. 1993, in ASP Conf. Ser. 46, IAU Colloq. 141: The Magnetic and Velocity Fields of Solar Active Regions, ed. H. Zirin, G. Ai, & H. Wang (San Francisco, CA: ASP), 11
Jess, D. B., Andić, A., Mathioudakis, M., Bloomfield, D. S., & Keenan, F. P. 2007, A&A, 473, 943
Jess, D. B., De Moortel, I., Mathioudakis, M., et al. 2012a, ApJ, 757, 160
Jess, D. B., Mathioudakis, M., Christian, D. J., Crockett, P. J., & Keenan, F. P. 2010a, ApJL, 719, L134
Jess, D. B., Mathioudakis, M., Christian, D. J., et al. 2010b, SoPh, 261, 363
Jess, D. B., Mathioudakis, M., Erdélyi, R., et al. 2009, Sci, 323, 1582
Jess, D. B., Pascoe, D. J., Christian, D. J., et al. 2012b, ApJL, 744, L5
Kobanov, N. I. 2000, SoPh, 196, 129
Kobanov, N. I., Kolobov, D. Y., & Makarchik, D. V. 2006, SoPh, 238, 231
Kobanov, N. I., & Makarchik, D. V. 2004, A&A, 424, 671
Langhans, K., Scharmer, G. B., Kiselman, D., & Löfdahl, M. G. 2007, A&A, 464, 763
Langhans, K., Scharmer, G. B., Kiselman, D., Löfdahl, M. G., & Berger, T. E. 2005, A&A, 436, 1087
Lawrence, J. K., Cadavid, A. C., Christian, D. J., Jess, D. B., & Mathioudakis, M. 2011, ApJL, 743, L24
Leenaarts, J., Carlsson, M., & Rouppe van der Voort, L. 2012, ApJ, 749, 136
Leka, K. D., Barnes, G., Crouch, A. D., et al. 2009, SoPh, 260, 83
Lites, B. W. 1992, in Proceedings of the NATO Advanced Research Workshop on the Theory of Sunspots, ed. J. H. Thomas & N. O. Weiss (Berlin: Springer), 261
Maltby, P., Avrett, E. H., Carlsson, M., et al. 1986, ApJ, 306, 284
Mathew, S. K., Solanki, S. K., Lagg, A., et al. 2004, A&A, 422, 693
Mathioudakis, M., Seiradakis, J. H., Williams, D. R., et al. 2003, A&A, 403, 1101
McEwan, M. P., Donnelly, G. R., Díaz, A. J., & Roberts, B. 2006, A&A, 460, 893
Metcalf, T. R., Leka, K. D., Barnes, G., et al. 2006, SoPh, 237, 267
Moreels, M. G., & Van Doorsselaere, T. 2013, A&A, 551, A137
Morton, R. J., Erdélyi, R., Jess, D. B., & Mathioudakis, M. 2011, ApJL, 729, L18
Morton, R. J., Verth, G., Jess, D. B., et al. 2012, NatCo, 3, 1315
Norton, A. A., Graham, J. P., Ulrich, R. K., et al. 2006, SoPh, 239, 69
Pesnell, W. D., Thompson, B. J., & Chamberlin, P. C. 2012, SoPh, 275, 3
Puschmann, K. G., Ruiz Cobo, B., & Martínez Pillet, V. 2010, ApJL, 721, L58
Reardon, K. P., Lepreti, F., Carbone, V., & Vecchio, A. 2008, ApJL, 683, L207
Reznikova, V. E., & Shibasaki, K. 2012, ApJ, 756, 35
Rimmele, T. R. 2004, Proc. SPIE, 5490, 34
Roberts, B., Edwin, P. M., & Benz, A. O. 1984, ApJ, 279, 857
Rouppe van der Voort, L. H. M., Rutten, R. J., Sütterlin, P., Sloover, P. J., & Krijger, J. M. 2003, A&A, 403, 277
Rudenko, G. V., & Anfinogentov, S. A. 2011, arXiv:1104.1228
Rutten, R. J. 2007, in ASP Conf. Ser. 368, The Physics of Chromospheric Plasmas, ed. P. Heinzel, I. Dorotovič, & R. J. Rutten (San Francisco, CA: ASP), 27
Schou, J., Scherrer, P. H., Bush, R. I., et al. 2012, SoPh, 275, 229
Solanki, S. K., Walther, U., & Livingston, W. 1993, A&A, 277, 639
Thomas, J. H., Cram, L. E., & Nye, A. H. 1982, Natur, 297, 485
Thomas, J. H., & Weiss, N. O. 2008, Sunspots and Starspots (Cambridge: Cambridge Univ. Press)
Torrence, C., & Compo, G. P. 1998, BAMS, 79, 61
Tziotziou, K., Tsiropoula, G., Mein, N., & Mein, P. 2006, A&A, 456, 689
Tziotziou, K., Tsiropoula, G., Mein, N., & Mein, P. 2007, A&A, 463, 1153
Uchida, Y. 1970, PASJ, 22, 341
Van Doorsselaere, T., Brady, C. S., Verwichte, E., & Nakariakov, V. M. 2008, A&A, 491, L9
Van Doorsselaere, T., Nakariakov, V. M., & Verwichte, E. 2007, A&A, 473, 959
Vernazza, J. E., Avrett, E. H., & Loeser, R. 1981, ApJS, 45, 635
Verwichte, E., Nakariakov, V. M., Ofman, L., & Deluca, E. E. 2004, SoPh, 223, 77
Weiss, N. O., Thomas, J. H., Brummell, N. H., & Tobias, S. M. 2004, ApJ, 600, 1073
Wöger, F., von der Lühe, O., & Reardon, K. 2008, A&A, 488, 375
Zirin, H., & Stein, A. 1972, ApJL, 178, L85